RASĀYAN *J. Chem.*
Vol. 19 | No. 3 | 1919-1927 | July-September | 2026
ISSN: 0974-1496 | e-ISSN: 0976-0083 | CODEN: RJCABP
http://www.rasayanjournal.com
http://www.rasayanjournal.co.in

NICKEL MANGANESE FERRITE NANOPARTICLES: A PLATFORM FOR SIMULTANEOUS ELECTROCHEMICAL SENSING OF DOPAMINE AND ERLOTINIB

D. M. Tejashwini[1], K. R. Mahanthesha[1,✉], K. R. Rajashekar[2], and C. T. Keerthi Kumar[1]

[1]Department of Studies in Chemistry, Shivagangothri, Davangere University, Davangere-577007, India

[2]Department of Studies in Physics, Davangere University, Shivagangothri, Davangere-577007, India

✉Corresponding author: krmahanthesha@gmail.com

ABSTRACT

Nickel manganese ferrite nanoparticle was synthesized via the conventional combustion method. XRD analysis confirms that the crystallite size of nickel manganese ferrite nanoparticle was found to be 24 nm. The bandgap was 2.27 eV as validated by UV-Visible spectroscopic analysis. The exterior morphology and elemental analysis of the synthesized nanoparticles was confirmed by SEM and EDAX analysis. Employing cyclic voltammetry and differential pulse voltammetry, the electrochemical performance of nickel manganese ferrite nanoparticles for the determination of neurotransmitters and anticancer drugs in the presence of biomolecules was studied. Varying the scan rate of the current-voltage cycle, anodic peak currents were recorded and studied, associated with neurotransmitters such as dopamine and anticancer drugs like erlotinib, in the presence of ascorbic acid. By employing a nickel manganese ferrite-based modified screen-printed electrode, it is feasible to know that the synthesized nanoparticles are an effective material for the electrochemical sensing of ascorbic acid, dopamine and erlotinib simultaneously. These findings highlight the potential application of nickel manganese ferrite-based modified screen-printed electrode in biosensing and clinical diagnostics. By offering an affordable, highly sensitive and selective platform for multi-analyte detection, these discoveries considerably enhance nanostructured ferrite electrochemical sensors. The work improves analytical reliability by addressing important simultaneous detection issues such as electrode stability and signal interference. Additionally, this study encourages further studies toward streamlined, real-time diagnostic systems by offering new directions for the fabrication of ferrite-based nanomaterials in biological sensing. The reported performance shows great promise for practical purposes in point-of-care testing, medication surveillance, and clinical diagnostics.

Keywords: Ascorbic Acid, Combustion Synthesis, Dopamine Sensing, Electrochemical Sensing, Erlotinib Sensing, Nickel Manganese Ferrite.

RASĀYAN*J. Chem.*, Vol. 19, No.3, 2026

INTRODUCTION

Transition metal oxides, specifically ferrite-based nanomaterials, have drawn substantial interest owing to their redox characteristics, structural adaptability, and significant promise for electrochemical sensing applications. The spinel crystal structure of ferrites, having the general formula MFe_2O_4 (where M = Ni, Mn, Zn, Fe), enables for effective electron transport and provides an extensive range of ferrite oxidation states (Fe^{+2}/Fe^{+3}), validating their excellent charge transfer efficiency, making them suitable for electrochemical sensors. Trimetallic systems with the combined elements of Ni, Mn, and Fe lead to nickel manganese ferrite (NMnF) nanoparticles (NPs), which offer an outstanding benefit over conventional ferrite forms. Integration of Mn^{+2} and Ni^{+2} in the spinel lattice, the outcome leads to greater electron mobility, increased surface area, and lattice distortion, leads to enhance the material's electrochemical behaviour, also extending their lifespan and efficiency.[3,4] Erlotinib is an effective targeted anticancer drug that works by inhibiting the function of the epidermal growth factor receptor (EGFR).[5] Recently, identifying physiologically relevant compounds, including erlotinib (ERL), dopamine (DA), and ascorbic acid (AA), has become increasingly essential. These molecules serve necessary functions in anticancer

This work is licensed under a CC BY 4.0 license.

drugs, neurotransmission, and antioxidant defense accordingly.[6,7] Since anticancer medication toxicity and therapeutic mechanism provide significant challenges to therapy, ERL and DA concentration in biological fluids must be evaluated in order to optimise dosage and achieve the best possible therapeutic benefits.[8] Thus, designing effective, highly sensitive, and selective electrochemical sensors for simultaneous as well as individual monitoring is critical in healthcare diagnosis, clinical surveillance, and point-of-care testing. Ferrites tend to be increasingly widespread for electrochemical sensing, but there are very few functional and affordable sensor systems that can employ NMnF nanoparticles to simultaneously detect anticancer medication like ERL in the presence of DA and AA. Solution combustion method was employed for synthesizing NMnF nanomaterials using citric acid as both a fuel serves as a fast and cost-effective method for producing phase-pure materials with specific composition.[9] Traditional sensing techniques are frequently expensive, have limited repeatability, and need extensive fabrication processes. Due to its low detection limits, quick reaction times, and convenience, electrochemical analysis provides an excellent replacement.[10,11] Screen-printed electrodes (SPE) are ideal platforms for using synthesized NMnF NPs as a modifier in practical applications owing to their mobility, ease of exterior modification, and affordable price.[12,13] In cyclic voltammetry (CV) and differential pulse voltammetry (DPV) investigations, these modified electrodes show better peak current responses and reduced overpotentials, implying effective electrocatalytic oxidation of targeted analytes like AA, DA and ERL in phosphate buffer solutions.[14] This work investigates the multianalyte sensing using NMnF NPs as a modifier, synthesized via solution combustion. NMnF NPs potential in multianalyte electrochemical sensing has been thoroughly investigated. The pioneering potential of NMnF-based modified screen-printing electrode in the developing domains of biosensing for a multianalyte system was analyzed. In order to address this crucial gap and advance beneficial uses in clinical diagnostics, the current work attempts to develop and assess NMnF-based modified SPE (NMnF/MSPE) for sensitive, selective, and simultaneous detection of AA, DA, and ERL.

EXPERIMENTAL

Material and Methods

The chemicals and reagents used in these studies are nickel nitrate hexahydrate (Ni $(NO_3)_2 \cdot 6H_2O$), manganese nitrate hydrate (Mn $(NO_3)_2 \cdot H_2O$), ferric nitrate nanohydrate (Fe $(NO_3)_3 \cdot 9H_2O$), and citric acid ($C_6H_8O_{11}$) sourced from SRL Chemicals, India., for the synthesis of the NMnF nanoparticle as an active material of the electrochemical sensor. Ascorbic acid, dopamine and erlotinib were purchased from BLD Pharma, India. Phosphate-buffered solution (PBS, pH 5.8 -7.4) were employed in the electrolytic solution's formulation. Sodium dihydrogen phosphate monohydrate (NaH_2PO_4) and di-sodium hydrogen phosphate anhydrous (Na_2HPO_4) sourced from Himedia.

Synthesis of NMnF NPs

Dissolving stochiometric quantities of nickel nitrate, manganese nitrate and ferric nitrate as an oxidizer and reducer, using citric acid, a homogeneous solution was prepared for the synthesis of $Ni_{(1-x)}Mn_xFe_2O_4$ NPs with three different Mn molar fractions (x=0.00, 0.50, and 1.00). The solution was subsequently dissolved using the least amount of distilled water while being stirred for 30 minutes and placing the homogenous redox mixture in the petri dish in a muffle furnace that has been preheated to 530 ^{0}C for 10 minutes for each NPs. The porous dust is then remained in the dish is crushed and calcined for four hours at 950 °C to eliminate any residual contaminants.[15-17]

Preparation of the NMnF/MSPE

NMnF/MSPE was developed through modifying a screen-printed working electrode with the drop-casting process. The synthesized NMnF NPs were stirred for over 30 minutes using a magnetic stirrer after being dispersed in the minimum quantity of water. Initially, 5 µL of NMnF NPs solution was drop-casted on the working electrode surface, then let dry at ambient temperature. The resultant electrode was used as NMnF/MSPE and was employed in further electrochemical investigations.[18]

RESULTS AND DISCUSSION

Figure-1(a) depicts the XRD patterns of NMnF NPs, which were used to determine their purity, crystal structure, and structural properties. The characteristic peaks at 19.0^0, 31.3^0, 36.8^0, 38.6^0, 43.0^0, 55.6^0,

59.3^0, 65.3^0, and 74.4^0 can be indexed to (111), (220), (311), (222), (400), (422), (511), (440), and (433) crystal planes of the XRD patterns have been verified with standard diffraction files for $NiFe_2O_4$ (NF) NPs, JCPDS Card No. 10-0325 and $MnFe_2O_4$ (MnF) NPs matching with JCPDS Card No. 10-0319 and NMnF.[19]

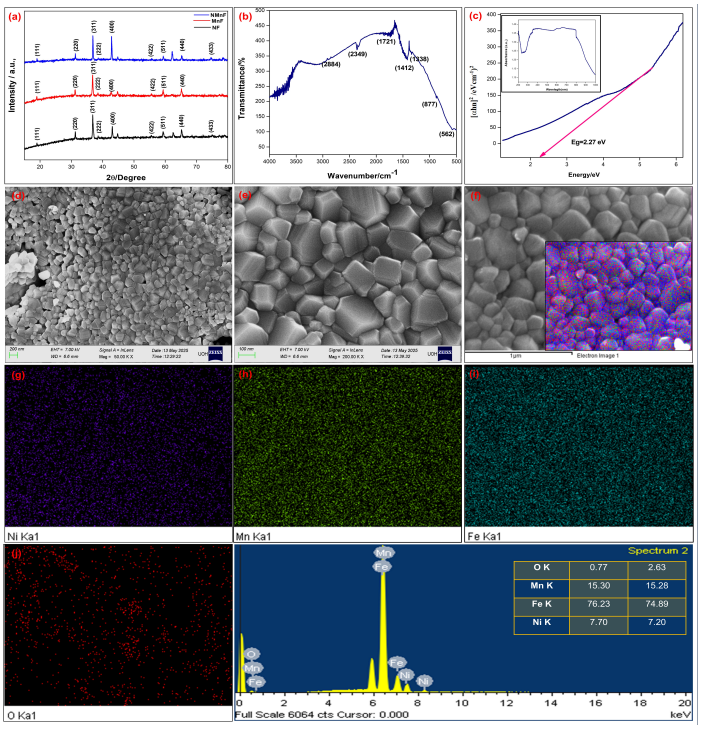

Fig.-1: (a) XRD Spectra of NMnF NPs, (b) FT-IR of NMnF NPs, (c) UV-Vis Spectroscopic Analysis of NMnF NPs, (d and e) SEM Images of NMnF NPs, (f to j) Colour Mapping of NMnF, Ni, Mn, Fe, and O (k) Elemental Mapping of NMnF

All three samples are identified as face-centered cubic spinal structure, and no impurity or secondary peaks are observed, confirming the successful synthesis of NF, MnF and pure single-phase NMnF NPs with the homogeneous spinel phase. The size of the crystallite 'D' for the synthesized NMnF NPs was determined using the Debye-Scherrer equation (1) and an experimentally proven broadening of among the most noticeable peaks in the diffraction X-ray spectrum.

$$D=K\lambda/\beta\cos\theta \quad (1)$$

The Lorentzian and Gaussian hindrances on form factors are 0.6366 and 0.9394. K is the Debye-Scherrer factor, which depicts the full width line at half maximum intensity (FWHM), the X-ray wavelength (Cu-K radiation = 1.5406), and the θ-Bragg angle, all expressed in radians.[20] The average crystallite size was computed using the Scherrer equation and three prominent diffraction peaks, resulting in average crystallite sizes of 35.3 nm for NF, 33.7 nm for MnF, and 24 nm for NMnF NPs. Synthesized NMnF NPs samples were evaluated using FT-IR spectroscopy at wavelengths between 400 and 4000 cm^{-1}, as illustrated in Fig.-1(b). Fe-O stretching vibrations at the tetrahedral site are suggested by the spectral peaks 562 cm^{-1} and 877 cm^{-1}. Approximately 1398 cm^{-1} has a distinct peak that might be related to the C–H vibration.[21] Carbonate groups (CO_3^{-2}) stretch symmetrically, as seen by the 1412 cm^{-1} band. The C=O stretching vibration of carboxylic groups, which may have resulted from residual citric acid fuel utilized during combustion, is accountable for the significant absorption at 1721 cm^{-1}. The C–H stretching vibration is linked to a large absorption band at 2349 cm^{-1} and 2884 cm^{-1} as shown in the Fig.-1(b).[22,23] The NMnF NPs was shown to cause a significant shift in the combined NPs absorbance toward the visible range (400–800 nm). The energy band gap (E_g) of the produced NMnF NPs was determined using the Tauc plot (Equation (2)), as shown in Fig.-1(c).

$$(\alpha h\nu)^n = (h\nu - E_g) \quad (2)$$

The absorption coefficient (*h*) is a function of photon energy, *n* indicates the electronic transition type, and E_g is the optical band gap energy. The specific electrical transition will determine the parameter n,

which often takes values like 1/2, 3/2, 2, and 3. Whereas n = 1/2 in a bandgap that is an indirect transition, n = 2 in a direct bandgap transition. This study used n = 2 to determine the optical energy bandgap of NMnF nanoparticle.[24,25] E_g decreased when NMnF was present in the heterostructure, indicating that the visible region's spectral response was affected. The analysis's findings indicate that the NMnF NPs exhibit 2.27 eV. The synthesized NMnF NPs surface morphology was examined using FE-SEM analysis. The SEM picture of the developed NMnF NPs is displayed in Fig.-1(d to e). According to the SEM image, the NMnF NPs are mostly quasi-cubic, with smooth surfaces and sharp angular edges. The particles seem to have great crystallinity due to their smoothness and density.[26] The uniform distribution of nickel, manganese, iron, and oxygen within the NPs was further confirmed by elemental mapping carried out in conjunction with SEM. As displayed in the Fig.-1(f to j), the synthesized NMnF NPs elemental distribution and composition were confirmed by means of colour mapping. Energy Dispersive X-ray Analysis (EDAX) analysis (Fig.-1(k)). These studies are crucial for validating the effective integration of the elements into the ferrite structure and ensuring their even distribution.[27]

Electrochemical Studies

Electrochemical Characterization of NMnF/MSPE Employing Standard Potassium Ferrocyanide System

The CV graphs were obtained for BSPE and NMnF/MSPE at 50 mV/s in an electrochemical cell containing freshly prepared 1mM potassium ferrocyanide ($K_4[Fe(CN)_6]$) in 1 M potassium chloride (KCl) as a suitable electrolyte, as shown in Fig.-2(a). Slow electron transfer kinetics were reported at 50 mV/s, leading to low peak current responses for BSPE and NMnF/MSPE. Anodic and cathodic peak potentials for BSPE were 0.238 V and 0.178 V, respectively, while for NMnF/MSPE, the values were 0.239 V and 0.181 V at 50 mV/s. BSPE and NMnF/MSPE had distinct redox peak potentials (ΔE_p) of 0.060 V and 0.058 V, respectively. Under the same electrolytic conditions, NMnF/MSPE exhibits a greater rise in redox peak currents, suggesting that the surface quality of the modified electrode has improved.

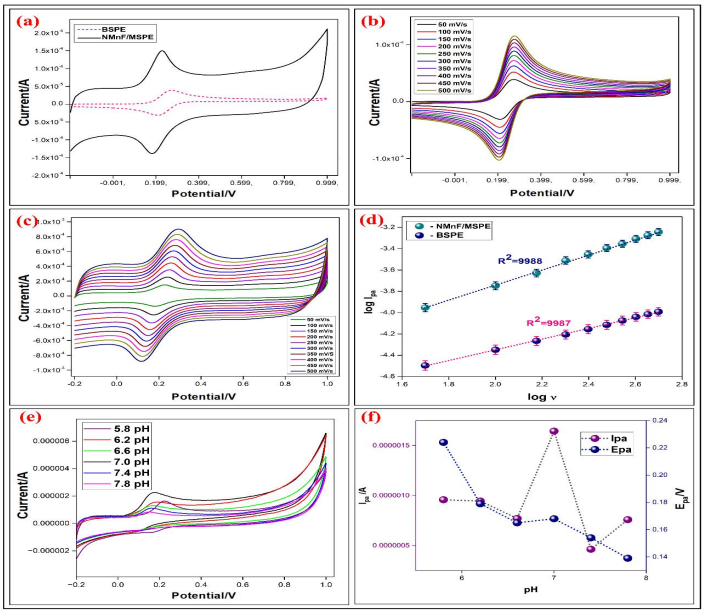

Fig.-2: (a) CV of BSPE (dashed line) and NMnF/MSPE (solid lines) for 1 mM $K_4[Fe(CN)_6]$ in 1M KCl solution at a scan rate of 50 mV/s (b) CV of BSPE (c) CV analysis of NMnF/MSPE from 50 mV/s to 500 mV/s (d) log I_{pa} versus log ν plot for BSPE and NMnF/MSPE (e) CV of oxidation of 10 µM DA in PBS of different pH from 5.8 to 7.8 for NMnF/MSPE (f) pH dependence on I_{pa} and plot of E_{pa} vs pH for NMnF/MSPE

Figure-2(b and c) displays the CV for BSPE and NMnF/MSPE at 50 mV/s to 500 mV/s under the same experimental conditions. A common method for determining the electroactive surface area of electrodes accessible for the reaction of species in a solution is the Randles-Sevcik equation (3).

$$I_p = 2.69 \times 10^5 \cdot n^{3/2} A D^{1/2} C_0 \nu^{1/2} \quad (3)$$

Where peak current is denoted by I_p (μA), *A* is the electroactive surface of the electrode, *n* is the overall number of electrons transferred, *D* is the diffusion coefficient of 1 mM $K_4[Fe(CN)_6]$ (cm^2/s), C_0 is the concentration, and ν is the scan rate (mV/s).[28] The obtained slope, computed electroactive surface area and roughness factor for BSPE and NMnF/MSPE are summarized in Table-1.

Table-1: ESA and RI for BSPE and NMnF/MSPE

Electrode	Slope(m)	ESA (cm^2)	RI
BSPE	0.505	0.681	9.51
NMnF/MSPE	0.717	0.968	13.63

Figure-2(d) depicts the log I_{pa} vs log ν plot to calculate the average electroactive surface area at scan speeds ranging from 50 mV/s to 500 mV/s. Electroactive surface area (ESA) of BSPE and NMnF/MSPE is determined as 0.681cm² and 0.961 cm², respectively. Nearly 1.412-fold enhancement in electroactive surface area and corresponding rise in the roughness factor (RI) are attributed to NMnF's ability to impart a porous structure with a large surface area that promotes effective electron transport across the electrode and the electrolyte.[29]

Effect of pH

The effect of pH was studied for the oxidation of 10μM DA in PBS at NMnF/MSPE has been thoroughly evaluated in the pH range of 5.8-7.8 at 50 mV/s, as displayed in the Fig.-2(e). Variations in solution pH have a significant effect on analyte electrocatalytic oxidation by influencing peak current and redox peak potentials. As pH rises, the oxidation peak potential changes to a more negative potential.[30] The anodic peak potential (E_{pa}) vs pH, followed by I_{pa} vs pH graphs are plotted as illustrated in the Fig.-2(f), which implies the detection of DA is a pH-dependent phenomenon. As the pH rose, the Ep decreased, indicating that the electrode's electrocatalytic activity was good at pH 7.0 compared to other pH solutions. Furthermore, the I_{pa} vs pH graph makes it evident that the largest sensitivity occurs at pH 7.0. Hence, pH 7.0 was selected as a suitable electrolyte for further investigation.

Electrochemical Response of AA, DA and ERL at NMnF/MSPE

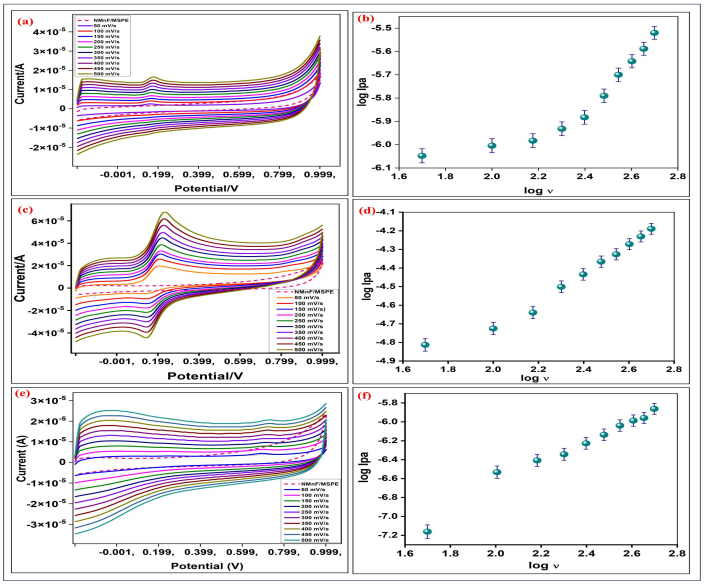

Fig.-3: CV of NMnF/MSPE of 10 μM (a)AA, (c) DA, (e) ERL from 50 to 500 mV/s in PBS at pH 7.0. Plot of log I_{pa} vs log ν for (b) AA, (d) DA and (f) ERL from 50 to 500mV/s

The anodic peak current of AA (10 μM), DA (10 μM) and ERL (10 μM) at NMnF/MSPE in pH 7.0 from 50 to 500 mV/s as shown in the Fig.-3(a, c, e). The E_{pa} moved to a slightly greater positive value as the scan rate increased. Graph of log I_{pa} vs. log ν was plotted over a similar scan rate range for AA, DA and ERL is shown in Fig.-3 (b,d,f), respectively.

The linear regression equation was-
$\log (I_{pa}) = 0.536 (\log \nu) - 7.072$, $r^2 = 0.891$ for AA,
$\log (I_{pa}) = 0.664 (\log \nu) - 6.015$, $r^2 = 0.9625$ for DA,
$\log (I_{pa}) = 1.177 (\log \nu) - 9.041$, $r^2 = 0.9632$ for ERL.
It demonstrated that the NMnF/MSPE's electron transfer reaction was a diffusion-controlled mechanism for AA and DA. Whereas for ERL, the electron transfer reaction was an adsorption-controlled mechanism.

Effect of Concentration of AA, DA and ERL at NMnF/MSPE

Figure-4 (a,c,e) demonstrates that the AA, DA and ERL concentrations are increased from 10µM to100 µM. The plot of I_{pa} of AA, DA and ERL vs concentration of AA, DA and ERL, respectively, displays increases in redox peak current at NMnF/MSPE, and it is almost good linearity as shown in Fig.-4 (b,d,f). I_{pa} rises as well, accompanied by the slight shift of E_{pa} towards less positive potential values, which signifies enhanced electron-transfer kinetics and efficient oxidation of AA, DA and ERL molecules over the electrode surface.[31]

I_{pa} (µA) = 2.243×10^{-8} (C_0 µmol/L) + 4.314×10^{-7}, $r^2 = 0.9524$ for AA,
I_{pa} (µA) = 2.294×10^{-7} (C_0 µmol/L) + 1.265×10^{-5}, $r^2 = 0.9875$ for DA,
I_{pa} (µA) = 7.807×10^{-8} (C_0 µmol/L) + 4.361×10^{-6}, $r^2 = 0.8789$ for ERL.

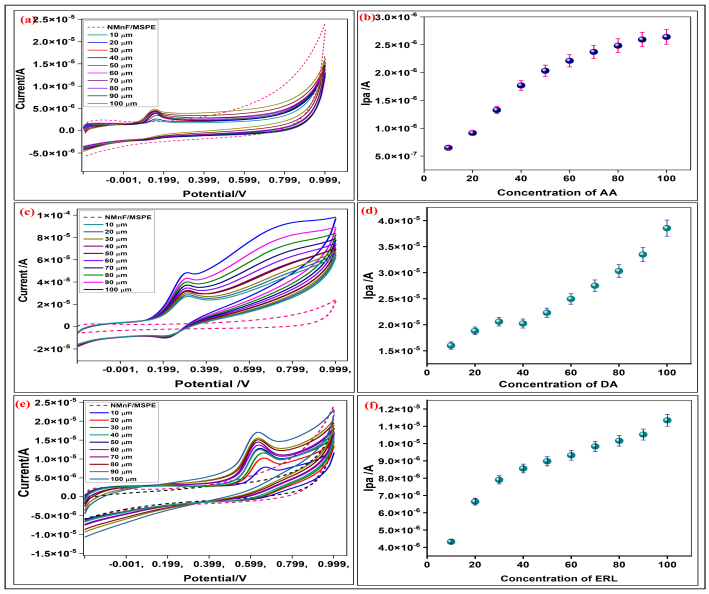

Fig.-4: CV of NMnF/MSPE from 10 µM to 100 µM of (a)AA, (c) DA, (e) ERL at 50 mV/s in pH 7.0, Graph of I_{pa} versus Concentration of (b) AA, (d) DA and (f) ERL at 50 mV/s.

The following equations (4) and (5) were used to compute the limit of quantification (LOQ) and limit of detection (LOD). For AA, LOD was 6.97 nM, and LOQ was 23.2 nM. DA's LOD and LOQ computed values are 0.682 nM and 2.27 nM, respectively, whereas for ERL's LOD and LOQ was 2.00 nM and 6.67 nM.

$$LOD = 3 (S/M) \quad (4)$$
$$LOQ = 10 (S/M) \quad (5)$$

Where M represents the calibration plot's slope, S is the five observations standard deviation for the blank signals. By DPV analysis, different concentrations of AA, DA, and ERL ranging from 10µM to 100µM in PBS with a pH of 7 as an appropriate electrolyte, as shown in the Fig.-4. BSPE (dashed line), NMnF/MSPE (dashed line) followed by addition of AA (Fig.-4(a)), DA (Fig.-4(c)), and ERL (Fig.-4 (e)) with a concentration range from 10µM to100µM at NMnF/MSPE.[32]

Simultaneous Investigation

The electrochemical behavior of a combination of 10µM AA, 10µM DA, and 10µM ERL was examined using a CV analysis to evaluate the selectivity and sensitivity of NMnF/MSPE. In Fig.-5(a), the CV for AA, DA, and ERL coexisting at BSPE (dashed line) lacks the capacity to differentiate the voltammetric

signals of AA, DA, and ERL. At around 0.27 V and 0.6 V, there was just two broad voltammetric signals for AA, DA, and ERL as a result of the fouling of oxidation products at the electrode surface.[33] Consequently, the DPV signal was resolved by the NMnF/MSPE into three distinct voltammetric peaks found at 0.15 V, 0.33 V and 0.58 V, which correspond to AA, DA, and ERL, respectively (solid line). AA and DA's oxidation peaks were distinguished by roughly 0.19 V.

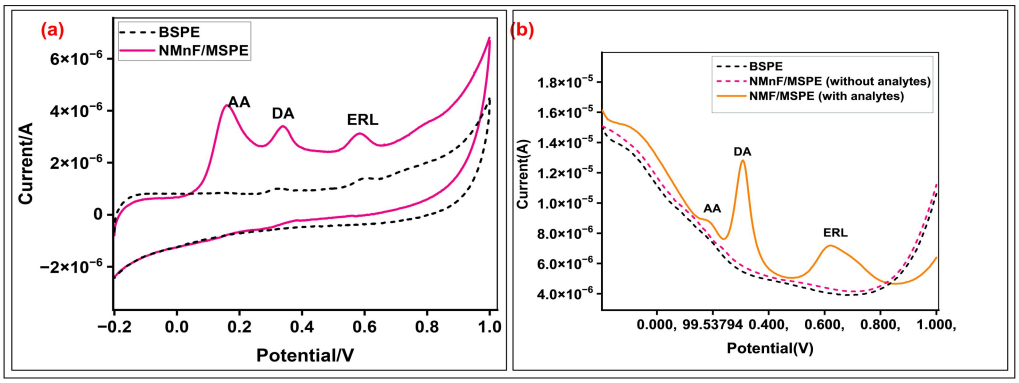

Fig.-5: (a) CV for 10µM AA, DA and ERL for BSPE (dashed line) and NMnF/MSPE (solid line) at the Scan Rate of 50 mV/s (b) DPV for 10µM AA, DA and ERL for BSPE (dashed line), NMnF/MSPE Without Analytes (dashed line) and NMnF/MSPE with Analytes (solid line) at 50 mV/s using pH 7.0 PBS

In contrast, ERL and AA's oxidation peaks were separated by around 0.24 V. AA, DA, and ERL concentrations at 10µM during the simultaneous analysis were simultaneously added and are shown in the Fig.-5(b). These findings demonstrated the existence and effective sensing of the AA, DA, and ERL at NMnF/MSPE.[34] SDG 3: Good Health and Well-Being is directly related to the current study. The development of NMnF/MPSE, which allows for the quick, accurate, and sensitive detection of hazardous analytes, supports this alignment. In addition to enhancing public health safety and supporting global efforts to guarantee healthy lives and promote wellness for all, such skills are essential for early diagnosis, environmental monitoring, and preventing health risks connected with contaminants. The current work advances the current reservoir of knowledge by revealing a relatively inexpensive and effective NMnF/MSPE with increased electroactive surface area and better electron transfer kinetics than BSPE. A significant problem in electrochemical sensing of co-existing analysers is addressed by NMnF/MSPR's capacity to concurrently detect AA, DA, and ERL with excellent sensitivity, selectivity, and well-resolved peak separation. These results offer a solid foundation for the fabrication of next-generation electrochemical sensors that could potentially find implementation in pharmaceutical evaluation and clinical diagnostics.

CONCLUSION

The research highlights chemically synthesized NMnF nanoparticles by combustion using citric acid as fuel for anticancer and neurotransmitter sensing. Formation of NMnF NPs with a spinel cubic structure with nanoscale crystallite sizes of roughly 24 nm was revealed by XRD analysis. The NPs with different functional groupings were verified by FTIR analysis, and the optical characteristics of the NPs was shown by UV-Vis analysis, showing a bandgap of 2.27 eV. FE-SEM images revealed the NMnF NP's external morphology, which increases their active surface area for electrochemical potential for charge transfer. NMnF/MSPE was used in electrochemical sensing applications, which shows the effective sensing of AA, DA, and ERL with the excellent LOD values. These results confirm NMnF/MSPE's adaptability as a durable biosensor in clinical diagnostics. The results of this work directly relate to SDG 3: The developed sensor for wellness and good health enables the sensitive and rapid detection of physiologically relevant analytes to support early diagnosis and enhanced medical monitoring.

ACKNOWLEDGMENTS

The author gratefully acknowledges the NFST Fellowship, awarded as per the official award no. 202324-NFST-KAR-01223, for supporting this research work.

CONFLICT OF INTERESTS

The authors declare that there is no conflict of interest.

AUTHOR CONTRIBUTIONS

The present work is related to *SDG-3: Good Health and Well-Being*. All the authors contributed significantly to this manuscript, participated in reviewing/editing and approved the final draft for publication. The research profile of the authors can be verified from their ORCID ids, given below:

D.M Tejashwini http://orchid.org/0009-0005-3341-2022
K.R Mahanthesha http://orchid.org/0000-0002-2034-1721
K.R Rajashekar http://orchid.org/0009-0009-1615-5609
C. T. Keerthi Kumar http://orchid.org/0000-0002-3184-8368

Open Access: This article is distributed under the terms of the Creative Commons Attribution 4.0 International License (http://creativecommons.org/licenses/by/4.0/), which permits unrestricted use, distribution, and reproduction in any medium, provided you give appropriate credit to the original author(s) and the source, provide a link to the Creative Commons license, and indicate if changes were made.
Cite this article as: D. M. Tejashwini *et al.*, *Rasayan J. Chem.*, 19(3), 1919-1927(2026), https://doi.org/10.31788/RJC.2026.1939822

REFERENCES

1. Y. Krishnan, K. Babu, S. Sakkaraiyan, A. Dinesh, A. Shanmugam, K. Radhakrishnan and M. Ayyar, *Semiconductors*, **58**, 721(2024), http://dx.doi.org/10.1134/S1063782624601808
2. T. N. Pham, N. X. Dinh, N. T. Lan, N. V. Quy, N. T. Bach, V. D. Lam and A. T. Le, *Journal of Alloys and Compounds*, **949**, 169880(2023), http://dx.doi.org/10.1016/j.jallcom.2023.169880
3. B. Aghalli, H. K. Fadafan and M. B. Najjar, *Physica E: Low-dimensional Systems and Nanostructures*, **165**, 116112(2025), http://dx.doi.org/10.1016/j.physe.2024.116112
4. L. Akbar, M. Ahmed, I. U. Haq, A. Nawaz and M. S. Bhutta, *Solid State Communications*, **378**, 115410(2024), http://dx.doi.org/10.1016/j.ssc.2023.115410
5. W. Du, Y. Zheng, X. Liu, J. Cheng, R. C. K. Reddy, A. Zeb and Y. Luo, *Chemical Engineering Journal*, **451**, 138626(2023), http://dx.doi.org/10.1016/j.cej.2022.138626
6. S. A. Ahmed, M. Roushani and Z. M. Karazan, *Microchim Acta*, **192**, 138(2025), http://dx.doi.org/10.1007/s00604-025-07012-4
7. X. Xu and X. Guo, *Microchemical Journal*, **212**, 113123(2025), http://dx.doi.org/10.1016/j.microc.2025.113123
8. H. Rahmanian, Z. Es'haghi and M. Dadmehr, *Nanotechnology*, **34**, 015502(2023), http://dx.doi.org/10.1088/1361-6528/ac8996
9. F. M. dos Santos Garrido, M. I. Argolo, M. E. Medeiros and J. M. Siqueira, *Current Nanoscience*, **17**, 505(2021), http://dx.doi.org/10.2174/1573413716999201106150041
10. R. Singh, R. Gupta, D. Bansal, R. Bhateria and M. Sharma, *ACS Omega*, **9**, 7336(2024), http://dx.doi.org/10.1021/acsomega.3c08060
11. X. Zhang, J. Chai, Y. Zhan, D. Cui, X. Wang and L. Gao, *Micromachines*, **16**, 330(2025), http://dx.doi.org/10.3390/mi16030330
12. M. H. Hassan, R. Khan and S. Andreescu, *Electrochemical Science Advances*, **2**, e2100184(2022), http://dx.doi.org/10.1002/elsa.202100184
13. K. Torres-Rivero, A. Florido and J. Bastos-Arrieta, *Sensors*, **21**, 2596(2021), http://dx.doi.org/10.3390/s21082596
14. A. Bazrafkan, F. G. Zaimbashi Nejad, R. Zaimbashi and H. Beitollahi, *Electrochemistry Communications*, **176**, 107928(2025), https://doi.org/10.1016/j.elecom.2025.107928
15. E. Carlos, R. Martins, E. Fortunato and R. Branquinho, *Chemistry-A European Journal*, **26**, 9099(2020), http://dx.doi.org/10.1002/chem.202000678
16. A. Varma, A. S. Mukasyan, A. S. Rogachev and K. V. Manukyan, *Chemical Reviews*, **116**, 14493(2016), http://dx.doi.org/10.1021/acs.chemrev.6b00279

17. T. Islam, M. M. Hasan, A. Awal, M. Nurunnabi and A. S. Ahammad, *Molecules*, **25**, 5787(2020), http://dx.doi.org/10.3390/molecules25245787
18. A. Vazhayil, J. Thomas and N. Thomas, *Journal of Electroanalytical Chemistry*, **936**, 117396(2023), http://dx.doi.org/10.1016/j.jelechem.2023.117396
19. I. Chicinaş, T. F. Marinca, B. V. Neamţu, F. Popa, O. Isnard and V. Pop, *IEEE Transactions on Magnetics*, **50**, 1(2014), http://dx.doi.org/10.1109/TMAG.2013.2285246
20. M. Sharma, S. Sundriyal, A. K. Panwar and A. Gaur, *Electrochimica Acta*, **294**, 53(2019), http://dx.doi.org/10.1016/j.electacta.2018.10.085
21. M. Hamid, M. Rianna, M. D. E. Vania, I. D. Yanti, F. A. A. Manurung, R. Afriandani and A. Daulay, *Materials Science for Energy Technologies*, **6**, 382(2023), http://dx.doi.org/10.1016/j.mset.2023.02.004
22. B. Souri, A. R. Rezvani, S. Abbasi, P. Hayati and R. Centore, *Inorganica Chimica Acta*, **498**, 119134(2019), http://dx.doi.org/10.1016/j.ica.2019.119134
23. M. Rudolph, J. Erler and U. A. Peuker, *Colloids and Surfaces A: Physicochemical and Engineering Aspects*, **397**, 16(2012), http://dx.doi.org/10.1016/j.colsurfa.2011.12.020
24. H. Badiger, B. G. Hegde, S. P. Kubrin, N. Chougala and S. Matteppanavar, *Journal of Material Science: Materials in Electronics*, **36**, 1576(2025), http://dx.doi.org/10.1007/s10854-025-15632-y
25. A. Nurmayansih, P. L. Hariani and M. Said, *Indonesian Journal of Fundamental and Applied Chemistry*, **6**, 115(2021), https://doi.org/10.24845/IJFAC.V6.I3.115
26. D. Ji, J. Sun, L. Tian, A. Chinnappan, T. Zhang, W. A. D. M. Jayathilaka and S. Ramakrishna, *Advance Functional Materials*, **30**, 1910568(2020), http://dx.doi.org/10.1002/adfm.201910568
27. P. Kumari, S. Thakur, G. Guleria, S. Thakur and S. Sharma, *Nano*, **18**, 2250113(2023), http://dx.doi.org/10.1142/S1793292022501132
28. R. B. Anagawadi, K. R. Mahanthesha and K. R. Rajashekar, *Journal of Alloys and Compounds Communications*, **11**, 100207(2026), http://dx.doi.org/10.1016/j.jacomc.2026.100207
29. T. Starodub and S. Michalkiewicz, *Materials*, **17**, 5864(2024), http://dx.doi.org/10.3390/ma17235864
30. N. R. Priya, K. R. Mahanthesha, R. B. Anagawadi and B. M. Sathosh, *Journal of Electrochemical Society*, **171**, 027522(2024), http://dx.doi.org/10.1149/1945-7111/ad2283
31. M. A. Bouicha, C. Mabrouk, B. Gassoumi, H. Barhoumi, M. A. Molton, F. Loiseau and H. Nasri, *RSC Advances*, **15**, 9810(2025), https://doi.org/10.1039/d5ra00762c
32. B. Kanthappa, J. G. Manjunatha, S. A. Aldossari and C. Raril, *Scientific Reports*, **15**, 5822(2025), https://doi.org/10.1038/s41598-025-90235-5
33. Y. Kandeepan and S. M. Chen, *Journal of Alloys and Compounds*, **1020**, 179315(2025), http://dx.doi.org/10.1016/j.jallcom.2025.179315
34. S. Singh, S. Singh, S. Afgan, P. Yadav, V. Ganesan and R. Kumar, *ACS Applied Polymer Materials*, **7**, 666(2025), https://doi.org/10.1021/acsapm.4c02924

[RJC-9822/2026]